Supporting Information

2D $NbIrTe_4$ and $TaRhTe_4$ Monolayers: Two Fascinating Topological Insulators as Electrocatalysts for Oxygen Reduction

Mingyue Lv,[a,#] Guangtao Yu[a,#] and Wei Chen[*abc]

[a]*Engineering Research Center of Industrial Biocatalysis, Fujian Provincial Key Laboratory of Advanced Materials Oriented Chemical Engineering, Fujian-Taiwan Science and Technology Cooperation Base of Biomedical Materials and Tissue Engineering, College of Chemistry and Materials Science, Fujian Normal University, Fuzhou, 350007, China*

[b]*Academy of Carbon Neutrality of Fujian Normal University, Fuzhou, 350007, China*

[c]*Fujian Provincial Key Laboratory of Theoretical and Computational Chemistry, Xiamen University, Xiamen, 361005, China.*

Email: chenwei@fjnu.edu.cn

#These authors contributed equally to this work.

Table of Contents

Figure S1: Free energy diagrams of oxygen reduction reaction by using (a) 5 × 5 × 1 k-points or (b) considering solvation effect for Paths I-1 and VI on the $NbIrTe_4$ monolayer.....3

Figure S2: Crystal structures of bulk $NbIrTe_4$ (a) and $TaRhTe_4$ (c). Note that Turquoise, dark blue, light blue, green and orange spheres represent Nb, Ir, Ta, Rh and Te atoms, respectively. The calculated cleavage energy of monolayers $NbIrTe_4$ (b) and $TaRhTe_4$ (d) by enlarging the interlayer distance between the exfoliated monolayer and the remaining four layers. 3

Figure S3: Electronic band structures of bulk $NbIrTe_4$ (a) and $TaRhTe_4$ (b). High-symmetric k-point paths: X (1/2, 0) → R (1/2, 1/2) → Y (0, 1/2) → G (0, 0) → X (1/2, 0).....4

Figure S4: Total energy as a function of time for $NbIrTe_4$ (a) and $TaRhTe_4$ (b) monolayers at 300 K during *ab initio* molecular dynamics. Insets: snapshots of the structure after 5 *ps*.....4

Figure S5: (Color online) Calculated orientation-dependent Youngs's modulus E(θ) and Poisson's ratioν (θ) of the $NbIrTe_4$ (a) and $TaRhTe_4$ (b) monolayers.....5

Figure S6: Density of states of $NbIrTe_4$ (a) and $TaRhTe_4$ (b) monolayers.....5

Figure S7: Optimized structures of optimal O_2 adsorption on $NbIrTe_4$ (a) and $TaRhTe_4$ (b) monolayers, as well as the distribution of charge difference of O_2 adsorbed on the $NbIrTe_4$ (c) and $TaRhTe_4$ (d) monolayers. Cyan and yellow colors denote charge depletion and accumulation, respectively. Partial density of states of $NbIrTe_4$ (e) and $TaRhTe_4$ (f) monolayers with adsorbing O_2 at the Te-site coordinated with three Nb/Ta atoms. The π* antibonding orbital of the adsorbed O_2 molecule on $NbIrTe_4$ (g) and $TaRhTe_4$ (h) monolayers.....6

Figure S8: (a) Optimized structures of O_2 adsorption at the edge sites of $NbIrTe_4$ and $TaRhTe_4$ systems as well as the corresponding adsorption energy (ΔE_{O2*}). Free energy diagrams of oxygen reduction at the zigzag [Te-Ir] edge (b) and the zigzag [Te-Nb] edge (c) of $NbIrTe_4$ and at the zigzag [Te-Rh] edge (d) of $TaRhTe_4$ at U=0 V. The corresponding structure diagrams are shown in the blank space. 7

Figure S9: Variation in the adsorption free energy of the adsorbates (ΔG_{OH*} and ΔG_{O*+OH*}), overpotential, the Bader charge as well as p-band center for the $NbIrTe_4$ (a, b) and $TaRhTe_4$ (c, d) monolayers. 8

Figure S10: Electronic band structures of pristine $NbIrTe_4$ monolayer and all intermediates along the dominant paths under dissociative mechanism and the corresponding electron density distributions (isovalue: 0.0008e/Bohr^3) near the Fermi level. 9

Figure S11: Electronic band structures of pristine $TaRhTe_4$ monolayer and all intermediates along the dominant paths under dissociative mechanism and the corresponding electron density distributions (isovalue: 0.0008e/Bohr^3) near the Fermi level. 10

Table S1: Gibbs adsorption free energy ΔG_{O*+O*} (eV) for 2D $NbIrTe_4$ and $TaRhTe_4$ monolayers and the corresponding Bader charge values (|e|).....11

Table S2: Each reaction equation of the dissociation paths and the corresponding free energy (ΔG) in eV for $NbIrTe_4$ and $TaRhTe_4$.The gray shadow represents the Gibbs free energy values of the rate-determining step.....11

Table S3: The ΔG_{OH*} values (eV) of subpaths 1, the ΔG_{O+OH*} values (eV) of subpaths 2, the corresponding Bader charge values (|e|) as well as the p-band center values (eV)for the $NbIrTe_4$ and $TaRhTe_4$ monolayers.....12

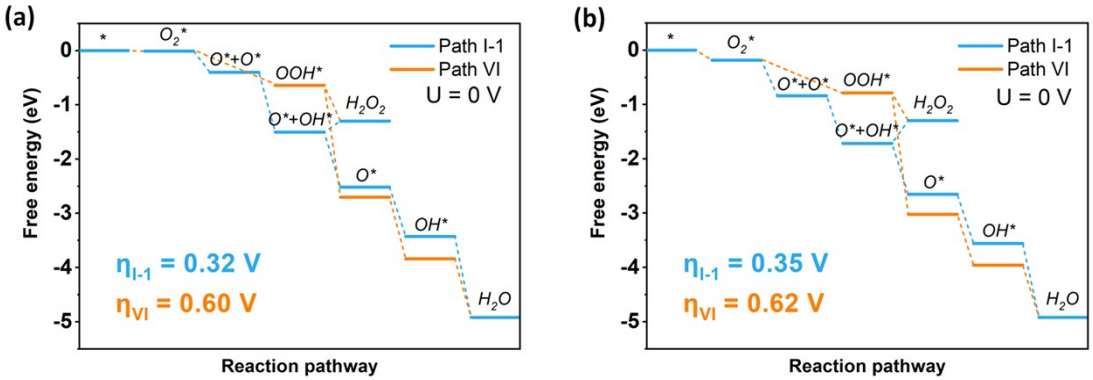

Figure S1. Free energy diagrams of oxygen reduction reaction by using (a) 5 × 5 × 1 k-points or (b) considering solvation effect for Paths I-1 and VI on the $NbIrTe_4$ monolayer.

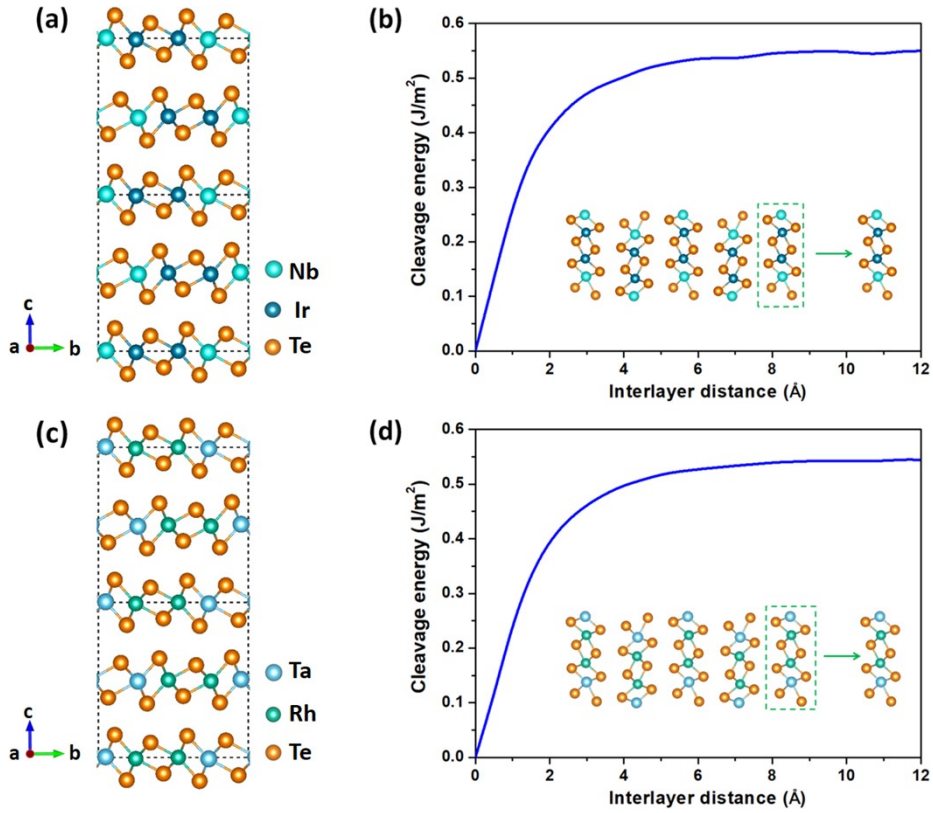

Figure S2. Crystal structures of bulk $NbIrTe_4$ (a) and $TaRhTe_4$ (c). Note that Turquoise, dark blue, light blue, green and orange spheres represent Nb, Ir, Ta, Rh and Te atoms, respectively. The calculated cleavage energy of monolayers $NbIrTe_4$ (b) and $TaRhTe_4$ (d) by enlarging the interlayer distance between the exfoliated monolayer and the remaining four layers.

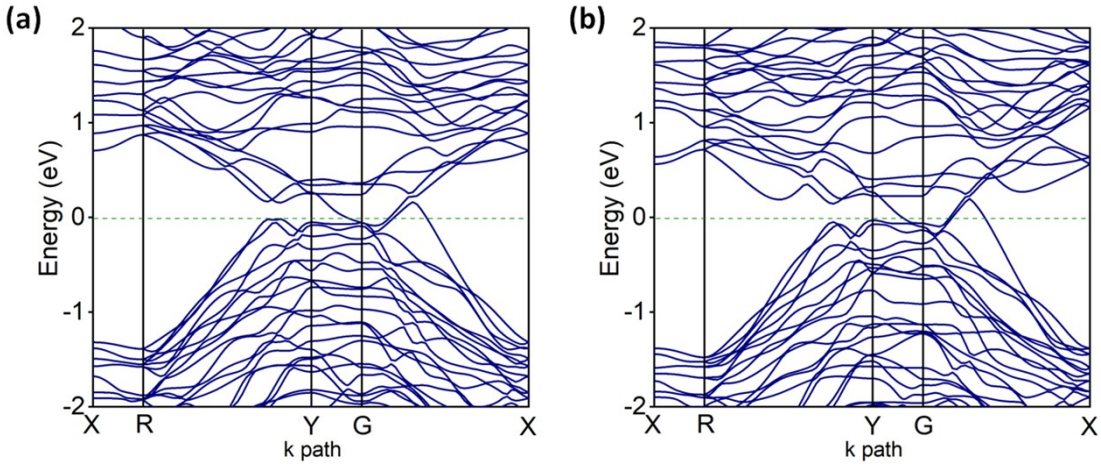

Figure S3. Electronic band structures of bulk $NbIrTe_4$ (a) and $TaRhTe_4$ (b). High-symmetric k-point paths: X (1/2, 0) → R (1/2, 1/2) → Y (0, 1/2) → G (0, 0) → X (1/2, 0).

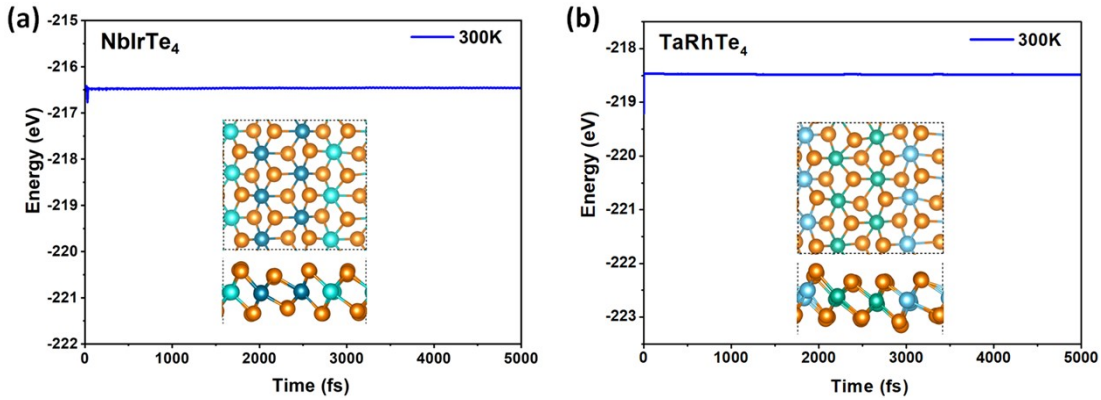

Figure S4. Total energy as a function of time for $NbIrTe_4$ (a) and $TaRhTe_4$ (b) monolayers at 300 K during *ab initio* molecular dynamics. Insets: snapshots of the structure after 5 *ps*.

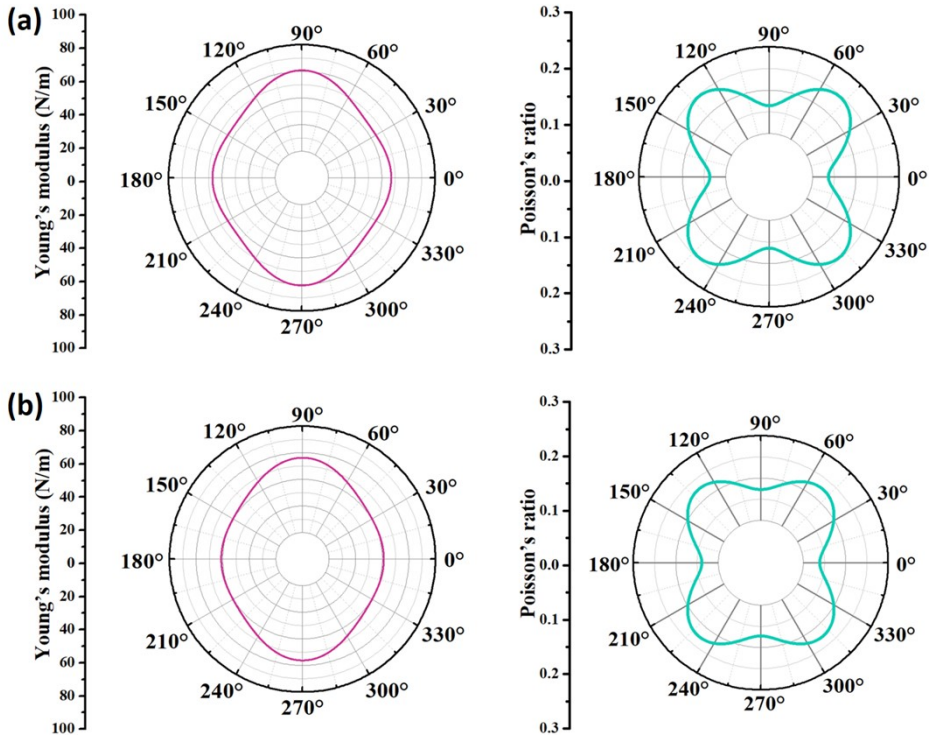

Figure S5. (Color online) Calculated orientation-dependent Youngs's modulus E(θ) and Poisson's ratiov (θ) of the $NbIrTe_4$ (a) and $TaRhTe_4$ (b) monolayers.

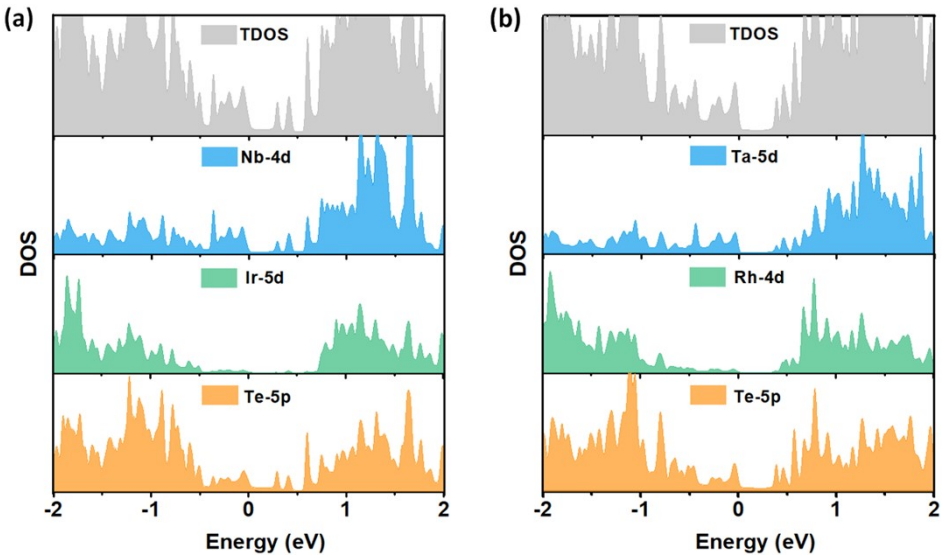

Figure S6. Density of states of $NbIrTe_4$ (a) and $TaRhTe_4$ (b) monolayers.

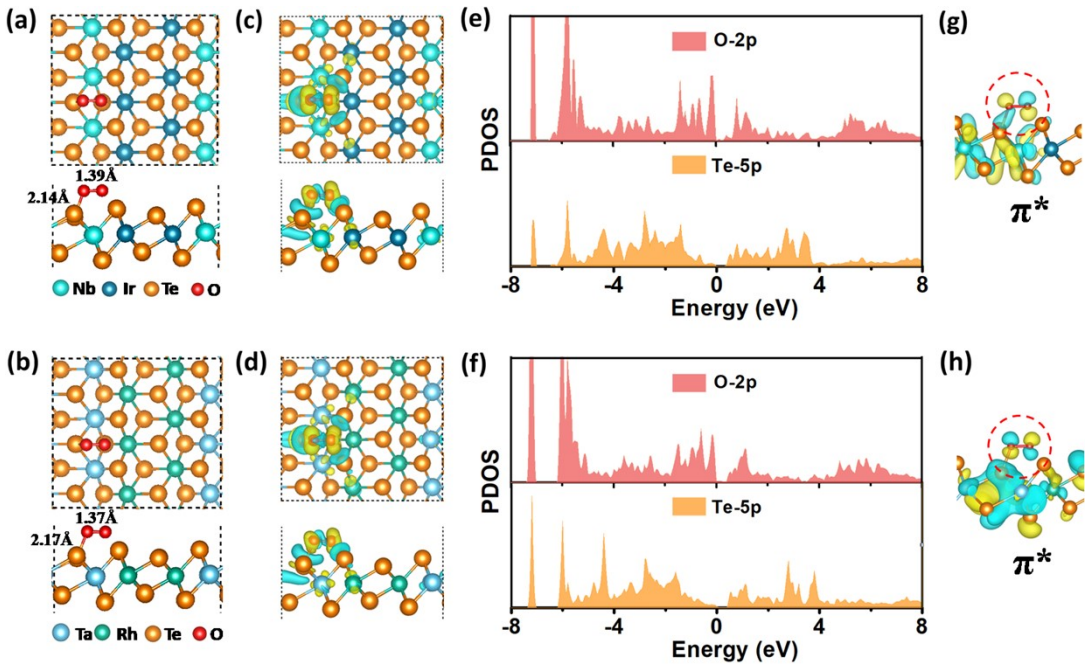

Figure S7. Optimized structures of optimal O_2 adsorption on $NbIrTe_4$ (a) and $TaRhTe_4$ (b) monolayers, as well as the distribution of charge difference of O_2 adsorbed on the $NbIrTe_4$ (c) and $TaRhTe_4$ (d) monolayers. Cyan and yellow colors denote charge depletion and accumulation, respectively. Partial density of states of $NbIrTe_4$ (e) and $TaRhTe_4$ (f) monolayers with adsorbing O_2 at the Te-site coordinated with three Nb/Ta atoms. The π^* antibonding orbital of the adsorbed O_2 molecule on $NbIrTe_4$ (g) and $TaRhTe_4$ (h) monolayers.

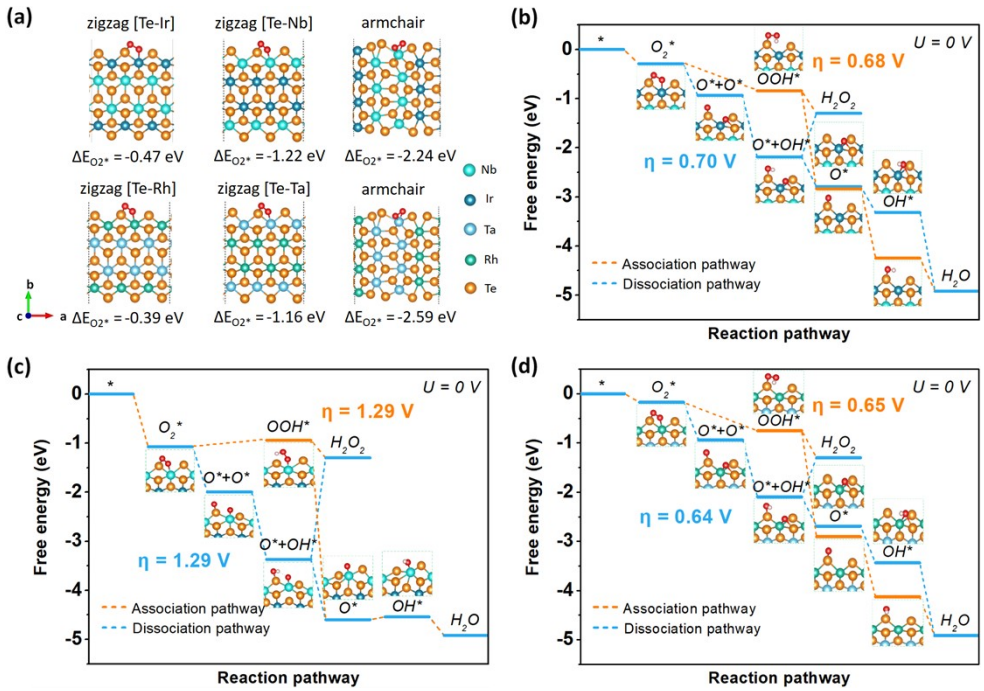

Figure S8. (a) Optimized structures of O_2 adsorption at the edge sites of $NbIrTe_4$ and $TaRhTe_4$ systems as well as the corresponding adsorption energy (ΔE_{O2*}). Free energy diagrams of oxygen reduction at the zigzag [Te-Ir] edge (b) and the zigzag [Te-Nb] edge (c) of $NbIrTe_4$ and at the zigzag [Te-Rh] edge (d) of $TaRhTe_4$ at U=0 V. The corresponding structure diagrams are shown in the blank space.

As shown in Fig. S8, we investigated the catalytic activity of oxygen reduction at the edge of $NbIrTe_4$ or $TaRhTe_4$, considering that the edge sites could also be the active centers. A total of three possible edges are considered for each system (Fig. S8a), namely, two zigzag edges with [Te-Ir] or [Te-Nb] chains and one armchair edge for $NbIrTe_4$, and two zigzag edges with [Te-Rh] or [Te-Ta] chains and one armchair edge for $TaRhTe_4$, respectively. Initially, we focused on the zigzag [Te-Ir] edge for $NbIrTe_4$, where the calculated oxygen adsorption energy is -0.47 eV. Further, the calculated overpotentials of dissociation and association paths are 0.70 V and 0.68 V, respectively (Fig. S8b), indicating that there is a certain catalytic activity of oxygen reduction, but it is obviously lower than the corresponding basal plane. In contrast, the remaining zigzag [Te-Nb] edge (-1.22 eV) and armchair edge (-2.24 eV) for $NbIrTe_4$ can possess too negative oxygen adsorption energy, suggesting that the adsorption strength at both edges is too strong. This can make it difficult for the subsequent oxygen reduction reaction to proceed, which is well reflected by the extremely large overpotential (1.29 V) of the sampled zigzag [Te-Nb] edge (Fig. S8c). Similarly, for $TaRhTe_4$, too strong oxygen adsorption can also occur at the zigzag [Te-Ta] edge (-1.16 eV) and the armchair edge (-2.59 eV), which is obviously unfavorable to oxygen reduction reaction. Therefore, we only focused on the zigzag [Te-Rh] edge for $TaRhTe_4$ system, which has the smallest oxygen adsorption energy (-0.39 eV). The calculated overpotentials of dissociation and association pathways on the zigzag [Te-Rh] edge are 0.64 and 0.65 V, respectively (Fig. S8d), indicating the existence of certain oxygen reduction activity, but it is far lower than the corresponding basal plane. Overall, the oxygen reduction activity at the edges of $NbIrTe_4$ and $TaRhTe_4$ can be much lower than the corresponding basal surfaces, due to the excessively strong oxygen adsorption.

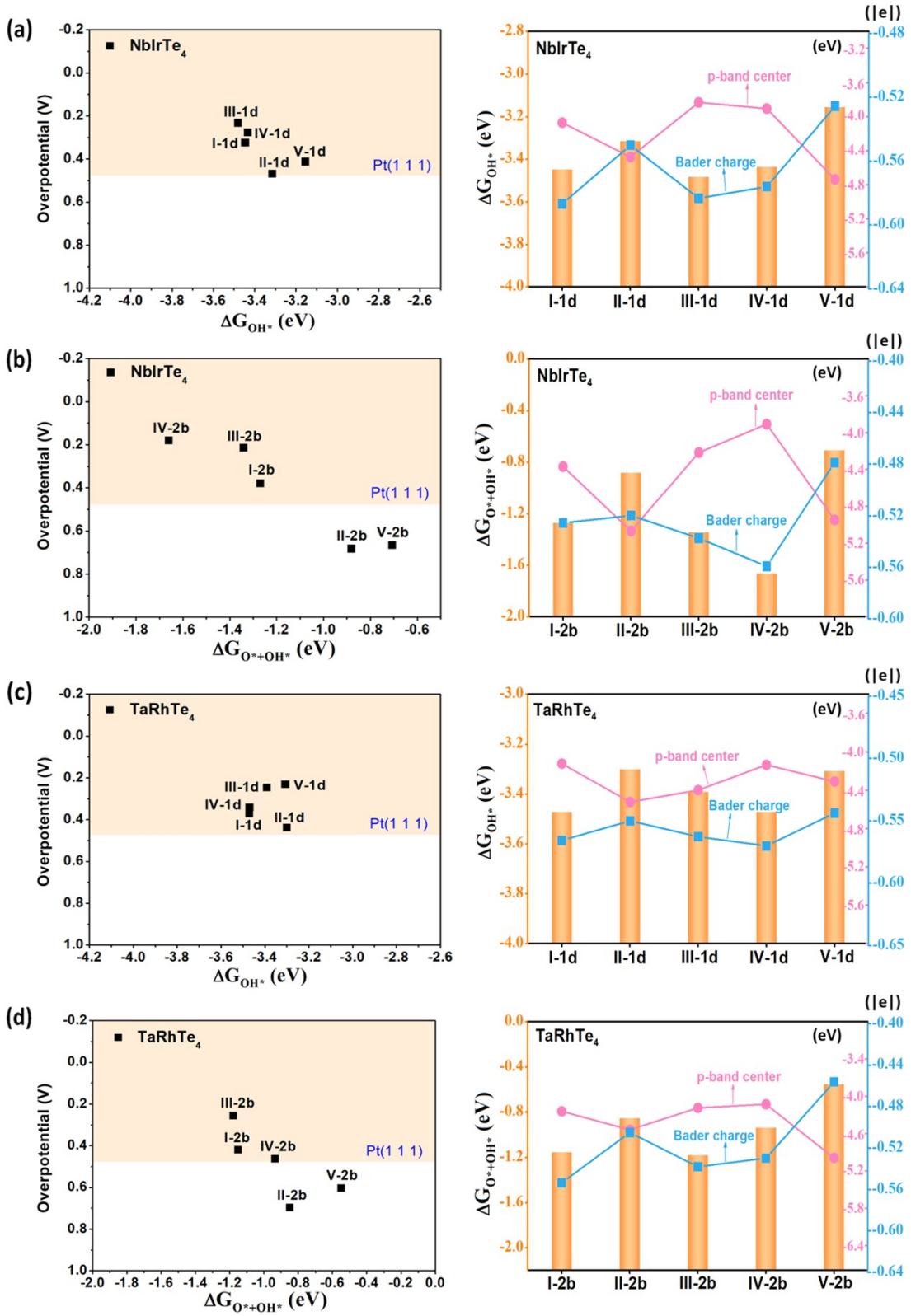

Figure S9. Variation in the adsorption free energy of the adsorbates (ΔG_{OH*} and ΔG_{O*+OH*}), overpotential, the Bader charge as well as p-band center for the $NbIrTe_4$ (a, b) and $TaRhTe_4$ (c, d) monolayers.

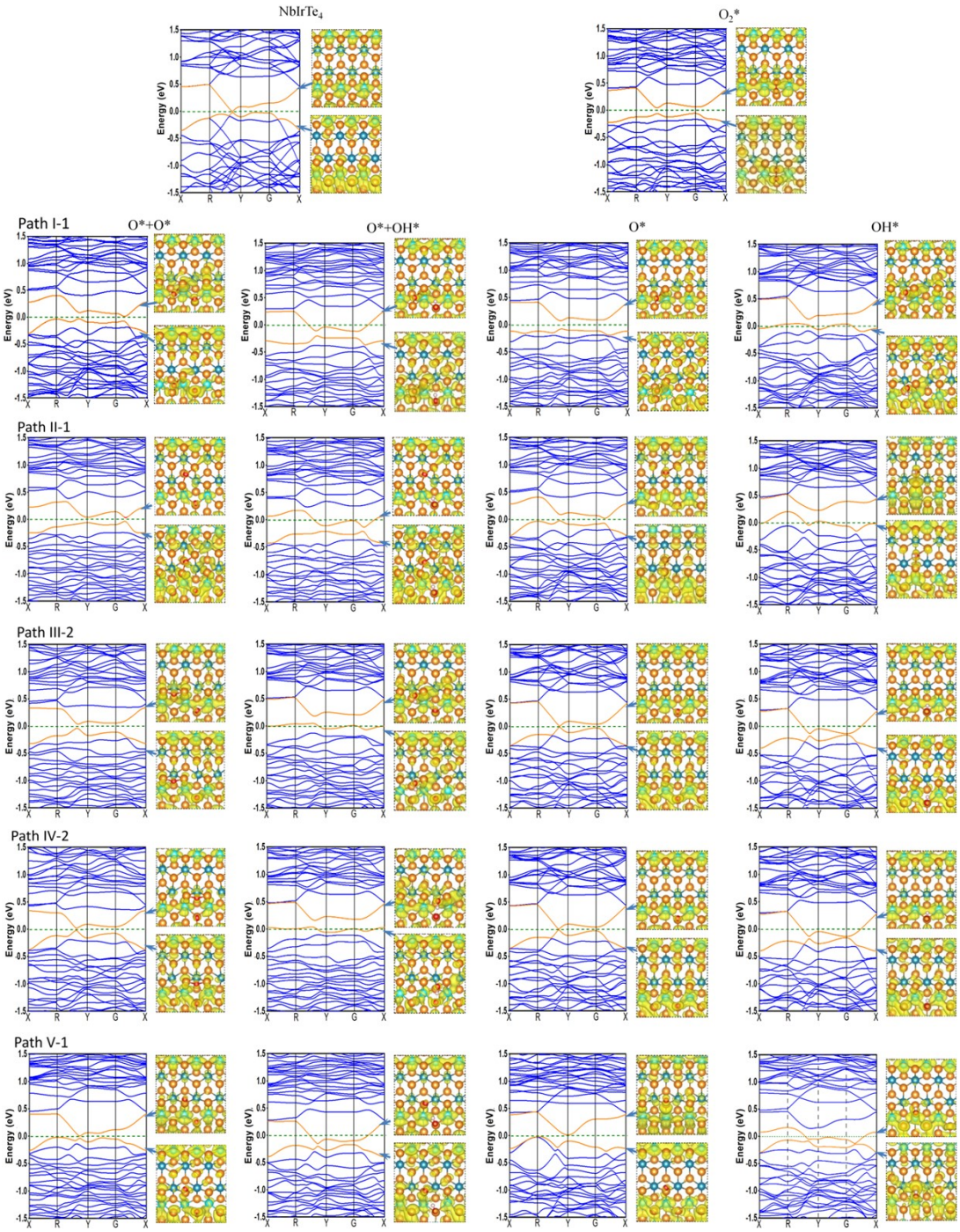

Figure S10. Electronic band structures of pristine $NbIrTe_4$ monolayer and all intermediates along the dominant paths under dissociative mechanism and the corresponding electron density distributions (isovalue: 0.0008e/Bohr^3) near the Fermi level.

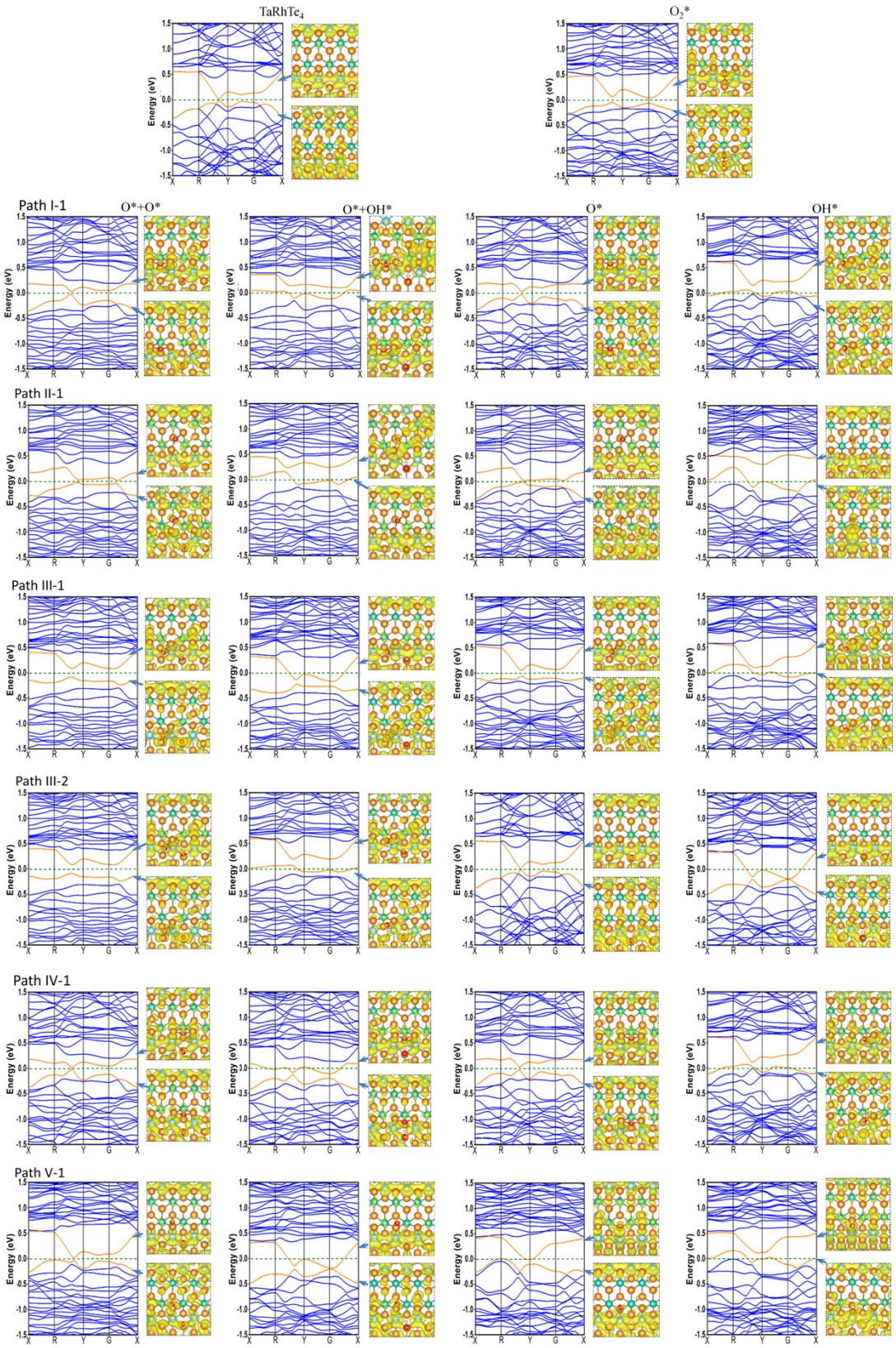

Figure S11. Electronic band structures of pristine $TaRhTe_4$ monolayer and all intermediates along the dominant paths under dissociative mechanism and the corresponding electron density distributions (isovalue: 0.0008e/Bohr^3) near the Fermi level.

Table S1 Gibbs adsorption free energy $\Delta G_{O^*+O^*}$ (eV) for 2D $NbIrTe_4$ and $TaRhTe_4$ monolayers and the corresponding Bader charge values (|e|).

Paths	$NbIrTe_4$		$TaRhTe_4$	
	$\Delta G_{O^*+O^*}$	Bader charge	$\Delta G_{O^*+O^*}$	Bader charge
I	-0.42	-1.98	-0.34	-1.97
II	-0.33	-1.96	-0.31	-1.97
III	-0.32	-1.95	-0.20	-1.91
IV	-0.20	-1.92	-0.17	-1.88
V	-0.14	-1.81	0.08	-1.83

Table S2 Each reaction equation of the dissociation paths and the corresponding free energy (ΔG) in eV for $NbIrTe_4$ and $TaRhTe_4$.The gray shadow represents the Gibbs free energy values of the rate-determining step.

	$NbIrTe_4$	I		II		III		IV		V	
	Reactionequation	I-1	I-2	II-1	II-2	III-1	III-2	IV-1	IV-2	V-1	V-2
(1)	$O_2^* \rightarrow O^* + O^*$	-0.39		-0.31		-0.30		-0.17		-0.12	
(2)	$O^* + O^* + H^+ + e^- \rightarrow O^* + OH^*$	-1.06	-0.85	-1.08	-0.55	-1.05	-1.02	-1.05	-1.46	-1.13	-0.56
(3)	$O + OH^* + H^+ + e^- \rightarrow O^* + H_2O$	-1.06	-1.44	-1.14	-1.83	-1.11	-1.37	-1.23	-1.05	-1.06	-2.00
(4)	$O^* + H^+ + e^- \rightarrow OH^*$	-0.91	-1.11	-0.76	-1.11	-1.00	-1.11	-0.95	-1.11	-0.82	-1.11
(5)	$OH^* + H^+ + e^- \rightarrow H_2O + *$	-1.47	-1.10	-1.61	-1.10	-1.44	-1.10	-1.49	-1.10	-1.77	-1.10
	Overpotentials	0.32	0.38	0.47	0.68	0.23	0.21	0.28	0.18	0.41	0.67
	$TaRhTe_4$	I		II		III		IV		V	
	Reactionequation	I-1	I-2	II-1	II-2	III-1	III-2	IV-1	IV-2	V-1	V-2
(1)	$O_2^* \rightarrow O^* + O^*$	-0.45		-0.43		-0.31		-0.28		-0.03	
(2)	$O^* + O^* + H^+ + e^- \rightarrow O^* + OH^*$	-0.99	-0.81	-1.02	-0.53	-1.05	-0.97	-1.51	-0.77	-1.02	-0.63
(3)	$O + OH^* + H^+ + e^- \rightarrow O^* + H_2O$	-1.29	-1.44	-1.17	-1.74	-1.15	-1.42	-0.90	-1.66	-1.36	-2.04
(4)	$O^* + H^+ + e^- \rightarrow OH^*$	-0.86	-1.02	-0.79	-1.02	-0.98	-1.02	-0.89	-1.02	-1.00	-1.02
(5)	$OH^* + H^+ + e^- \rightarrow H_2O + *$	-1.45	-1.30	-1.62	-1.30	-1.53	-1.30	-1.45	-1.30	-1.61	-1.30
	Overpotentials	0.37	0.42	0.44	0.70	0.25	0.26	0.34	0.46	0.23	0.60

Table S3 The ΔG_{OH*} values (eV) of subpaths 1, the ΔG_{O+OH*} values (eV) of subpaths 2, the corresponding Bader charge values (|e|) as well as the p-band center values (eV)for the $NbIrTe_4$ and $TaRhTe_4$ monolayers.

Paths	$NbIrTe_4$			$TaRhTe_4$		
	ΔG_{OH*}	Bader charge	p-band center	ΔG_{OH*}	Bader charge	p-band center
I-1	-3.45	-0.59	-4.07	-3.47	-0.57	-4.12
II-1	-3.31	-0.55	-4.47	-3.30	-0.55	-4.52
III-1	-3.48	-0.58	-3.83	-3.38	-0.56	-4.40
IV-1	-3.43	-0.58	-3.90	-3.47	-0.57	-4.13
V-1	-3.15	-0.53	-4.74	-3.31	-0.54	-4.31
Paths	ΔG_{O+OH*}	Bader charge	p-band center	ΔG_{O+OH*}	Bader charge	p-band center
I-2	-1.27	-0.54	-4.37	-1.15	-0.55	-4.44
II-2	-0.88	-0.52	-5.07	-0.85	-0.50	-4.74
III-2	-1.35	-0.54	-4.21	-1.18	-0.54	-4.37
IV-2	-1.66	-0.56	-3.91	-0.94	-0.53	-4.33
V-2	-0.70	-0.48	-4.95	-0.55	-0.46	-5.19